

Regulating the anion solvation and cathode-electrolyte interphase to improve the reversibility and kinetics of high-voltage dual-ion batteries

Shuang Wu^{a,1}, Xin Gu^{a,1,*}, Yang Li^a, Fengchun Li^a, Zhenjie Cheng^c, Qian Yao^b, Jian Yang^{b,*}, Dandan Liu^a, Liangjun Li^a, Pengcheng Dai^a, Mingbo Wu^{a,*}

^a College of New Energy, State Key Laboratory of Heavy Oil Processing, China University of Petroleum (East China), Qingdao 266580, PR China

^b Key Laboratory of Colloid and Interface Chemistry, Ministry of Education, School of Chemistry and Chemical Engineering, Shandong University, Jinan 250100, PR China

^c Institute of Electrochemistry, School of Materials Science and Engineering, Taizhou University, Taizhou 318000, PR China

ARTICLE INFO

Keywords:

Dual-ion batteries
Graphite cathode
Electrolyte
Solvation structure
Cathode-electrolyte interphase

ABSTRACT

The development of high-voltage dual-ion batteries (DIBs) is greatly hindered by the structure degradation of graphite cathodes during the (de-)intercalation of bulky anions, the electrolyte oxidative decomposition at high voltages, and inadequate cathode-electrolyte interphase (CEI) protection. Here, 1,1,2,2-tetrafluoroethyl-2,2,3,3-tetrafluoropropyl ether (TTE) is introduced as an electrolyte additive, which preferentially enters into the first shell structure of PF₆⁻ solvation, contributing to high oxidation stability of the electrolyte and formation of an inorganic LiF-rich CEI layer. This layer stabilizes the graphite structure and enhances the anion (de-)intercalation reversibility and transport kinetics. Consequently, the Li||graphite half cell with TTE in the electrolyte exhibits an ultrahigh rate capability (95.6 % at 30 C) and a remarkable capacity retention (67.6 % after 5000 cycles). The impressive performance is further demonstrated in the graphite||graphite full cell, showcasing exceptional cycle stability (91.9 % after 1000 cycles). This study underscores the significance of anionic solvent chemistry and CEI components on cathode materials for DIBs.

1. Introduction

Over the years, high-energy and long-lasting lithium-ion batteries (LIBs) have expanded their territory from consumer electronics to electric vehicles. However, the grid and utility applications of LIBs are severely limited by the availability and cost of lithium, nickel, and cobalt resources. [1,2] Dual-ion batteries (DIBs) featuring graphite cathodes are considered one of the most appealing alternatives to LIBs for their cost-effectiveness, high operating voltage, and rapid intercalation kinetics. [3-5] However, graphite cathodes (de-)intercalate anions at a potential higher than 4.5 V versus Li⁺/Li, which causes continuous electrolyte oxidative decomposition and low Coulombic efficiency (CE ≤ 95 %). [6,7] Furthermore, graphite cathodes suffer a significant volume expansion of over 130 % upon the intercalation of bulky anions, which damages cathode-electrolyte interphase (CEI) layers, causes structural deterioration of graphite cathodes, and results in severe capacity decline with prolonged cycling. [8-10] Therefore, improving the oxidation resistance of electrolytes and building stable CEI layers are crucial to

enhancing the cycling stability of graphite cathodes. [11]

The modulation of electrolyte compositions is highly sought after because it can improve electrochemical stability against oxidation, form stable interphase layers, and/or alter the anion intercalation process. [12-15] For instance, Xiang et al. reported a 7.5 M lithium bis(fluorosulfonyl)imide (LiFSI) in the carbonate electrolyte with 96.8 % capacity retention after 500 cycles. [16] Li et al. reported a 4 M LiFSI in the tetramethylene sulfone (TMS) electrolyte with a high oxidation potential of 6.0 V. [17] However, the high costs, viscosity, and low conductivity of highly concentrated electrolytes (HCEs) hinder their practical use. [18,19] On the other hand, Wang et al. used lithium difluoro(oxalate) borate (LiDFOB) as an additive to form a stable CEI, enabling a capacity retention of 87.5 % after 4000 cycles. [20] We designed a thin and robust CEI on graphite using the tris(trimethylsilyl) phosphite (TMSP) additive, improving the CE, capacity, and cycling stability. [21] Despite these achievements, the anion solvation and its impact on electrochemical stability and interphase chemistry have been largely ignored in the context of cathode materials that involve anion

* Corresponding authors.

E-mail addresses: guxin@upc.edu.cn (X. Gu), yangjian@sdu.edu.cn (J. Yang), wumb@upc.edu.cn (M. Wu).

¹ These authors are co-first authors and contributed equally to this work.

intercalation in DIBs. [19,22,23] Therefore, it is crucial to study anion solvation to gain valuable insights into the reversible anion (de-)intercalation and to develop new electrolytes.

A typical fluoro ether, 1,1,2,2-tetrafluoroethyl-2,2,3,3-tetrafluoropropyl ether (TTE), has been widely used as a non-solvating diluent in HCEs to reduce the viscosity while keeping similar local Li^+/Na^+ ion solvation structures, ensuring the long-term cycling stability and reliability of lithium/sodium batteries. [24,25] In this work, we present TTE as an electrolyte additive to regulate the anion solvation structures for DIBs for the first time. We find that TTE preferentially enters into the first shell structure of PF_6^- solvation, contributing to the high electrolyte stability at high voltages and forming an inorganic LiF-rich CEI layer on the cathode. This robust CEI layer on graphite cathodes effectively mitigates the electrolyte oxidative decomposition at high voltages and suppresses the significant volume change upon prolonged cycling. As a result, Li||graphite with TTE additive in the electrolyte exhibits a high capacity retention of 67.6 % over 5000 cycles and an ultrahigh rate capability of 95.6 % at 30 C. The study highlights the importance of anion solvation on electrochemical stability and interphase chemistry in DIBs.

2. Results and discussion

We first appraise the impact of TTE as an electrolyte additive on the electrochemical performance of Li||graphite. Fig. 1a illustrates the first charge/discharge voltage profiles of Li||graphite with and without TTE in the basic electrolyte (BE, 3 M LiPF_6 in EMC), and both profiles exhibit similar voltage patterns, consistent with the anion (de-)intercalation processes in graphite cathode. [26-28] This similarity suggests that the TTE additive does not alter the fundamental electrochemical reactions. However, the presence of TTE notably improves the first discharge capacity and the initial Coulombic efficiency (ICE), as depicted in Fig. 1b. These results imply that TTE enhances the electrochemical activity and mitigates side reactions. Furthermore, this positive influence is sustained in the subsequent cycles, as shown in Fig. 1c. After several cycles, the CE stabilizes at above 96 % for the BE with TTE, while the CE for the BE reaches only ~94 %.

Although the difference in CE between the two scenarios is slight, repeated cycling leads to a significant decline in electrochemical performance, as shown in Fig. 1d and S1. While cycling at 5 C, the specific capacity in the BE drops sharply from 80.1 to 40.7 mAh g^{-1} after 1000 cycles. However, when TTE is present in the BE, the specific capacity remains at 57.1 mAh g^{-1} even after 5000 cycles. This indicates an impressive retention rate of 67.6 %, which highlights the significant role

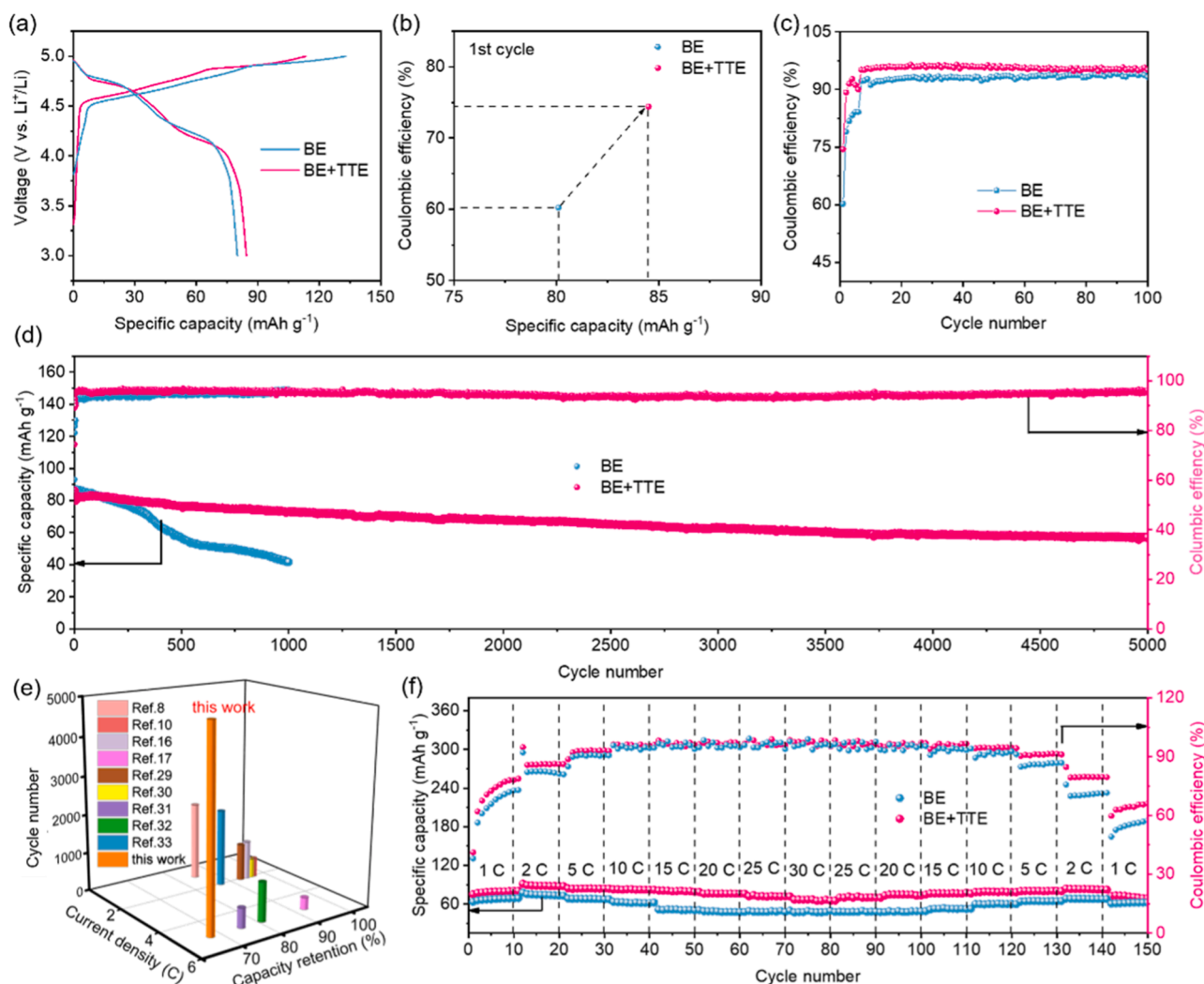


Fig. 1. (a) The first charge/discharge voltage profiles and (b) initial Coulombic efficiencies of Li||graphite using different electrolytes at 2 C (1 C = 100 mA g^{-1}). (c) The Coulombic efficiencies and (d) cycling performance of Li||graphite using different electrolytes at 5 C with the first five cycles at 2 C. (e) Comparison of the cycling performance with the reported data in DIBs. (f) Rate performance of Li||graphite using different electrolytes.

of TTE in enhancing the capacity retention of the battery. As shown in Fig. 1e, our cycling performance exceeds many of the previously reported outcomes for DIBs. [8,10,16,17,29-33] We tested various TTE concentrations in the basic electrolyte. Based on our findings, a 3 % TTE concentration showed the best electrochemical activity and cycle life-span (Fig. S2). Hence, all further discussions about TTE effects are based on a 3 % concentration. The voltage profiles of Li||graphite at different rates can be seen in Fig. S3, and Fig. 1f compares the rate capability of the cell with and without TTE in the BE. It is worth noting that the specific capacity of the cell with TTE in the BE only slightly decreases as the current density increases from 1 to 30 C. The specific capacity achieves 71.9 mAh g^{-1} at 30 C, 95.6 % of the data observed at 1 C. In contrast, the cell without TTE in the BE suffers a rapid reduction in capacity to 57.9 mAh g^{-1} at 30 C, which represents only 76.1 % of the capacity at 1 C. These results confirm that the presence of TTE increases the reaction kinetics of the cell. As discussed later, TTE induced the formation of thinner CEI layer and reduced by-products, contributing to a smaller interfacial ohmic impedance, enhancing the reaction kinetics. It is essential to determine whether the improved performance in the Li||graphite system is due to the effect of TTE on lithium metal. [19] The electrochemical properties of the symmetric cells based on lithium metals were thoroughly studied. Fig. S4 shows that symmetrical cells with and without TTE in the BE exhibit the same electrochemical performance. This finding effectively rules out any correlation between the

effects of TTE on lithium and the observed enhancement in performance in the Li||graphite system.

To validate the effectiveness of the TTE additive, we put together Li||graphite pouch cells and examined their performance during cycling at 5 C. The Li||graphite pouch cell sustains a capacity of 73.9 mAh g^{-1} after 400 cycles (Fig. S5a and S5b). The Coulombic efficiency remains stable at around 97 %, and the charge/discharge curves consistently maintain good reversibility over multiple cycles.

We employed electrochemical impedance spectroscopy (EIS) to clarify the underlying insights for the enhanced reaction kinetics of the graphite cathode with TTE in the BE. The EIS spectra for graphite with and without TTE were compared, revealing similar Nyquist plots (Fig. 2a). These plots show a semicircle that represents the impedances of the CEI (R_{CEI}) and charge transfer (R_{ct}) at the interface between the electrode and the electrolyte. There is also a straight line that corresponds to the Warburg impedance (Z_w). [34] Upon the addition of TTE, both R_{CEI} and R_{ct} decrease, as shown in Fig. 2b. This decrease indicates an improvement in charge transfer dynamics. The reduction in these values can be attributed to a thinner CEI layer and less by-product formation when TTE is present. Furthermore, the relationship between Z' (Z_{Re}) and $\omega^{-1/2}$ in the low-frequency (Fig. S6) suggests that the graphite cathode with TTE has a significantly improved anion diffusion coefficient of $4.55 \times 10^{-11} \text{ cm}^2 \text{ s}^{-1}$ compared to that without TTE (Fig. 2c), which is only $2.64 \times 10^{-11} \text{ cm}^2 \text{ s}^{-1}$.

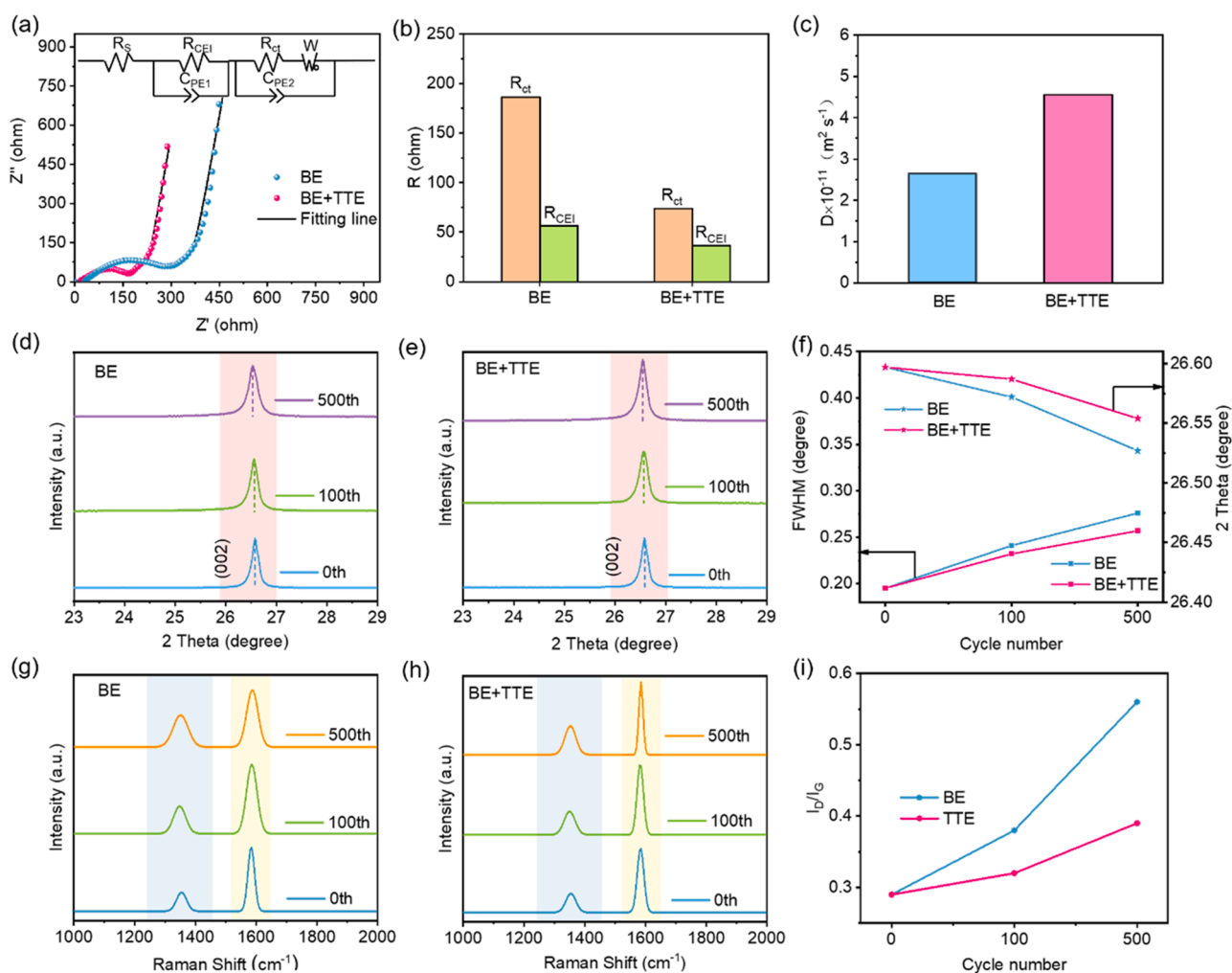


Fig. 2. (a) Nyquist plots of Li||graphite with different electrolytes after 100 cycles and the equivalent circuit. (b) Fitting parameters for the equivalent circuit. (c) Calculated ion diffusion coefficient with different electrolytes. XRD patterns of graphite in Li||graphite before and after different cycles using BE (d) and BE+TTE (e). (f) Full width at half maximum (FWHM) and peak position of the (002) peak of graphite cycled in different electrolytes. Raman spectra of graphite before and after different cycles using BE (g) and BE +TTE (h). (i) I_D/I_G of cycled graphite with cycles in different electrolytes.

The crystal structure of graphite in Li||graphite was monitored using X-ray diffraction (XRD) and Raman spectroscopy to uncover insights into the improved cycling stability facilitated by TTE. Fig. 2d and Fig. 2e show that graphite's (002) peak gradually becomes broader and shifts to a lower angle after cycling, regardless of whether TTE is added to the BE. The shift in the (002) peak to a lower angle implies an increase in the interlayer spacing, while the broadening of the (002) peak indicates a decrease in the order degree. These changes mean that anion/solvent molecules have left in graphite during cycling. [35] The results for both cases suggest that TTE does not entirely suppress these changes. However, in the absence of TTE, these changes are more pronounced than with TTE in the BE (Fig. 2f). This observation suggests that TTE enhances graphite's reversibility of anion/solvent intercalation. The conclusion that graphite without TTE addition has more significant structural damage is also supported by the Raman spectra (Fig. 2g-i). The peak ratio of I_{D/I_G} among these spectra is commonly used to evaluate the degree of graphitization in carbon materials. A higher I_{D/I_G} ratio indicates more severe damage to graphite. [36] Therefore, it can be concluded that graphite without TTE addition has a more pronounced structural damage (Fig. 2i), which is consistent with the higher irreversibility observed in this scenario.

We used atomic force microscopy (AFM) measurements to assess the interfacial morphology and mechanical strength of the CEI layer formed with and without TTE in the BE. [37] The measurements were conducted on the graphite cathode after 100 cycles. Planar images of the graphite cathode cycled in different electrolytes are shown in Fig. S7. Many residues are observed on the graphite surface developed in the BE due to severe electrolyte decomposition and structure breakage. Fig. 3a and Fig. 3b display the 3D images of the graphite surface developed with and without TTE in the BE. It is evident that the graphite cycled with BE shows a fluctuating morphology and a rough surface with an average roughness (Ra) of 179 nm. On the other hand, the graphite cycled with TTE in the BE exhibits a relatively uniform surface with a Ra of 118 nm. These results suggest that severe electrolyte decomposition results in an uneven CEI layer. [38] Fig. 3c and Fig. 3d show Fig. 3D images of the modulus distribution of the CEI layer formed in the BE with and without TTE. In the BE, the modulus distribution of the CEI layer was broad, with an average modulus of approximately 5.4 GPa. However, the CEI layer formed with TTE in the BE exhibits a narrow and concentrated modulus distribution, with an average modulus of 11.6 GPa. This value is more

than twice the average modulus of the CEI layer without TTE. Adding TTE to the electrolyte has improved the CEI layer by enhancing its morphology and mechanical properties. Consequently, this has led to faster reaction kinetics and enhanced structural stability. [39].

High-resolution transmission electron microscopy (HRTEM) was used along with AFM to observe the CEI layer directly. Fig. 3e and Fig. 3f are the HRTEM images of the graphite surface with and without TTE in the BE after 100 cycles. Notably, the graphite cathode cycled in the BE shows a non-uniform and thick CEI layer with a 14 to 25 nm thickness. In contrast, a uniform and thin CEI layer of approximately 9 nm is observed on the graphite cathode cycled with TTE in the BE. The modifications made on the graphite surface were also observed using scanning electron microscopy (SEM). Fig. S8 exhibits the graphite cathode with and without TTE after 100 cycles. Notably, the graphite cycled in the BE has many nanoparticles on the surface, which may be formed due to structural damage and electrolyte decomposition. [40] On the other hand, the graphite cycled with TTE in the BE has a smooth surface, indicating that detrimental impacts are effectively prevented. These pieces of evidence demonstrate the crucial role of TTE additives in forming a high-quality CEI layer on the cathode surface, preventing structural damage and adverse reactions between the reactive substance and the electrolyte. [41].

The depth profiles of X-ray photoelectron spectroscopy (XPS) were used to characterize the CEI components on graphite cathode after 100 cycles in different electrolytes. Fig. 4a-c and S9 show that the CEIs generated by these two electrolytes contain various species, including C—C, C—O, C=O, Li_2CO_3 , Li_xPF_y , $\text{Li}_x\text{PO}_y\text{F}_z$, and LiF. Overall, the TTE-contained electrolyte-derived CEI shows reduced C and O atomic ratios compared to the BE (Fig. S10), indicating fewer organic species generated by solvent decomposition. It also shows a reduced P atomic ratio compared to the BE, suggesting the addition of TTE inhibited the oxidative decomposition of PF_6^- anions. Additionally, it has been observed that the LiF content in the CEI increases significantly when TTE is added, indicating the formation of a LiF-rich CEI layer. The inner content of LiF with TTE-contained electrolyte reaches up to 5.9%, while that of the BE is only 3.3% (Fig. 4c). This result indicates that the fluoro-ether TTE probably participates in forming CEI and contributes to the high LiF content. As a result, this LiF-rich CEI layer acts as an optimal barrier that protects the graphite cathode from the harmful effects of HF and other free radical groups in the electrolyte. This helps to prevent

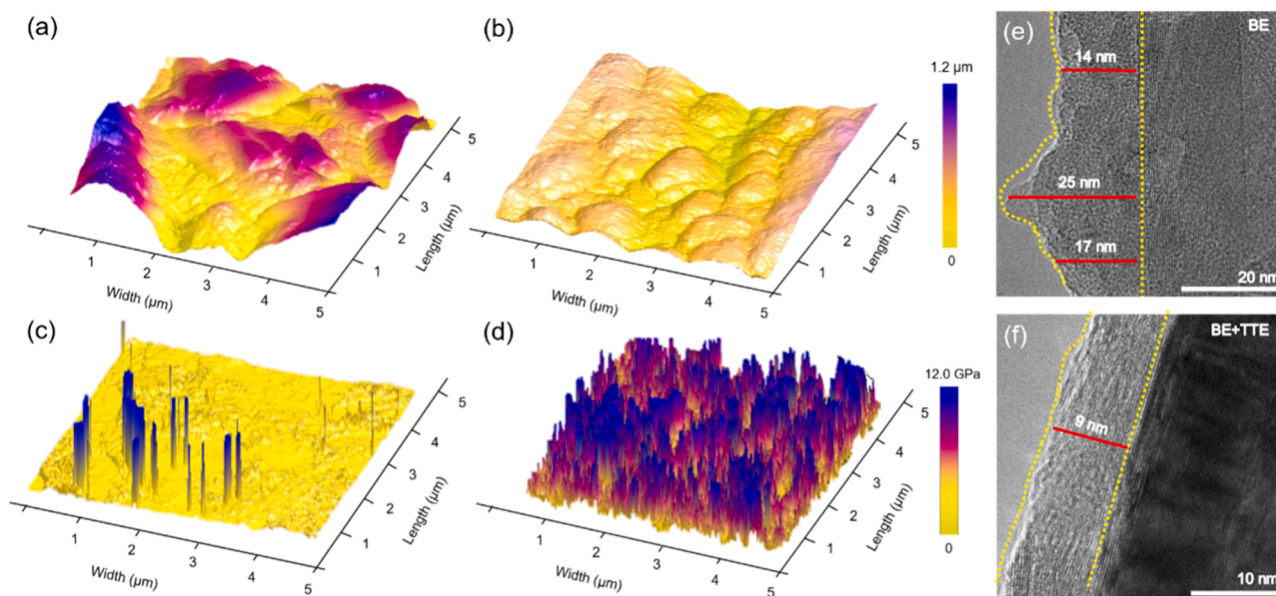


Fig. 3. AFM height images of the graphite surface after 100 cycles with BE (a) and BE+TTE (b). AFM DMT Modulus images of the graphite surface after 100 cycles with BE (c) and BE+TTE (d). HRTEM images of the graphite surface after 100 cycles with BE (e) and BE+TTE (f).

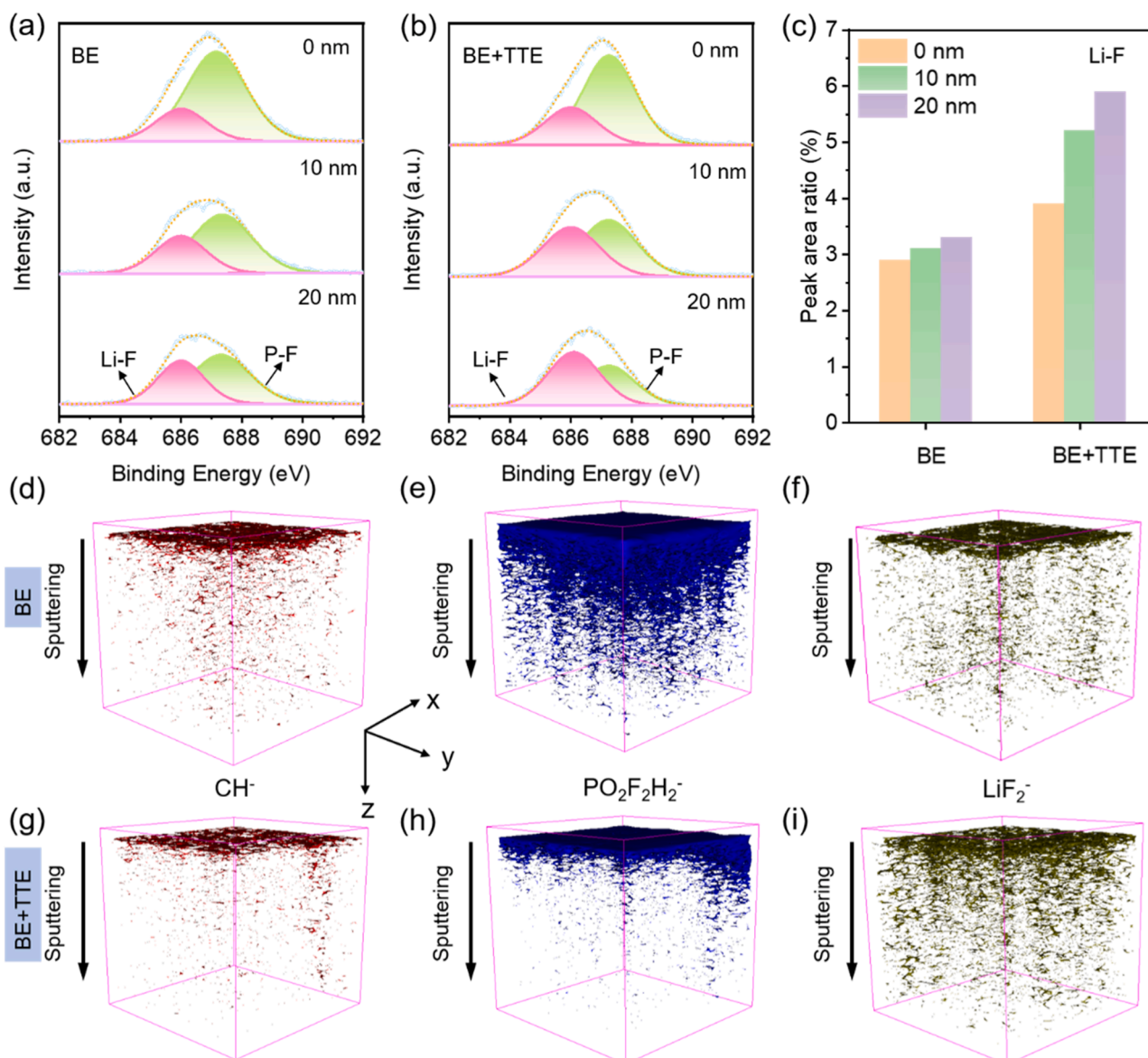


Fig. 4. The CEI components analysis of the graphite cathode after 100 cycles by XPS and ToF-SIMS. F 1 s of CEI formed in BE (a) and BE+TTE (b) at different depths. (c) LiF ratios of CEI formed in two electrolytes at different depths. 3D reconstructed images of ToF-SIMS for several representative secondary ions with BE (d-f) and BE+TTE (g-i).

undesirable side reactions. [42,43]

Time-of-flight secondary ion mass spectrometry (ToF-SIMS) was used to further confirm the components and distribution of CEI with a sputtered depth of 50 nm. The images in Fig. 4d-f show the 3D spatial distribution of several representative secondary ions (CH^- , $\text{PO}_2\text{F}_2\text{H}_2^-$, and LiF_2^-) from the CEI developed with BE. The CH^- fragment represents the solvent-generated organic component, while $\text{PO}_2\text{F}_2\text{H}_2^-$ and LiF_2^- fragments represent the inorganic species of phosphate and LiF, respectively. [44] The components of the CEI developed with TTE-contained electrolyte are similar to those of BE (Fig. 4g-i). However, the CEI generated by TTE-contained electrolyte presents lower signal intensity of CH^- and $\text{PO}_2\text{F}_2\text{H}_2^-$ than that in the BE. This result is consistent with the XPS results and confirms the inhibited decomposition of solvent and PF_6^- anions. Additionally, more LiF species are distributed throughout the entire CEI in the TTE-contained electrolyte than in the BE. These results indicate that using a TTE-contained electrolyte allows the graphite surface to create an inorganic LiF-rich CEI. This significantly improves the homogeneity and mechanical strength of the CEI. [45]

To gain a detailed understanding of the solvated structure of electrolytes with different TTE contents, we used nuclear magnetic resonance (NMR), Raman, and Fourier transform infrared (FTIR) spectroscopy measurements. In the ^{19}F NMR spectra (Fig. 5a), several new peaks appeared, and their intensity increased with the increasing TTE concentration, indicating an increase in the ionic dipole interaction between TTE and PF_6^- . [19,46] In addition, a downfield trend can be observed from the ^{19}F and ^{31}P NMR peaks of PF_6^- after the addition of TTE in electrolytes (Fig. 5b and Fig. 5c), which is an indication of the stronger binding between PF_6^- anions and TTE or an increased ion-pairing. [19,33] In the Raman spectra (Fig. S11a), the $\text{O}-\text{CH}_3$ vibration at $\approx 940\text{ cm}^{-1}$ is assigned to the free EMC. It shifts to a higher wavelength of 950 cm^{-1} , indicating that as the TTE increases, the EMC molecules solvate to Li^+ ions. [25,27] The FTIR spectra are displayed in Fig. S11b, showing a decrease in the ratio of free EMC to PF_6^- and the solvation of EMC with increasing TTE content. This is in line with the Raman results. [27,47]

We employed molecular dynamics (MD) simulations and density functional theory (DFT) calculations to elucidate the formation

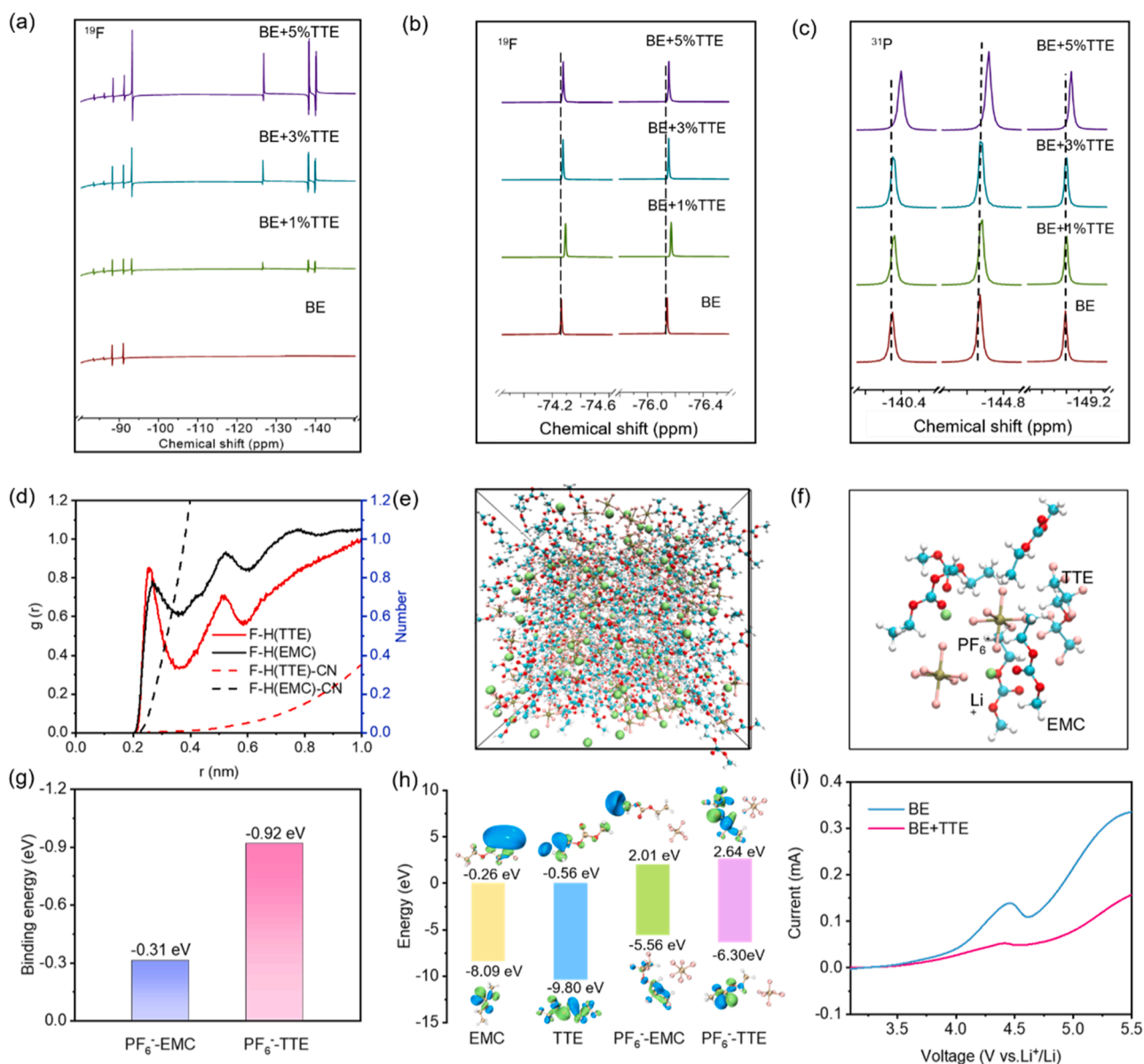


Fig. 5. Chemical shifts of ^{19}F spectra (a, b) and ^{31}P spectra (c) of BE, BE+1 % TTE, BE+3 % TTE and BE+5 % TTE. (d) The $g(r)$ and coordination number of BE+TTE electrolyte obtained by MD simulation. (e) End-state model of the simulated system. (f) Typical solvated structure. (g) The binding energy of PF_6^- with EMC and TTE. (h) The molecular orbital energy levels of EMC, TTE, PF_6^- -EMC, and PF_6^- -TTE. (i) The LSV curves of $\text{Li}||\text{stainless steel}$ cells with BE and BE+TTE electrolytes at a scan rate of 0.1 mV s^{-1} .

mechanism of the CEI. The interaction between TTE and anion/cation is first elucidated through the electrostatic potential (ESP) density distribution. Specifically, the negative F and positive charge H atoms in the TTE molecule tend to interact with Li^+ and PF_6^- , respectively (Fig. S12). [48] Then, the interaction between TTE and PF_6^- in the electrolyte was simulated by MD. Fig. 5d shows that the first peak of the radial distribution function of F-H (TTE) appeared at a position smaller than that of F-H (EMC). The F-H refers to F from PF_6^- and H from TTE or EMC. This suggests that TTE has entered the first shell structure of PF_6^- solvation. Additionally, the $g(r)$ intensity of F-H (TTE) is 0.85, higher than that of F-H (EMC), indicating a strong interaction of TTE in the first solvation shell of PF_6^- . The coordination number of PF_6^- with TTE is low. This happens because the concentration of the additive directly affects its interaction with the central atom. Fewer atoms can form coordination bonds with the central atom when the concentration is lower, reducing the solvated coordination number. [19,49] The VMD (Visual Molecular Dynamics) software was used to create the end-state model of the

simulated system. Fig. 5e shows the output of this model, while Fig. 5f shows the solvated structure containing TTE, EMC, Li^+ , and PF_6^- . This is further supported by the binding energy of PF_6^- with EMC and TTE, as shown in Fig. 5g. [50] This strong interaction between PF_6^- and TTE reduces the solvent EMC on the surface of the cathode. It increases the local stability of the electrolyte near the cathode, thereby suppressing the anodic oxidation decomposition and contributing to forming a LiF -rich CEI. The molecular orbital energy levels of EMC, TTE, PF_6^- -EMC, and PF_6^- -TTE were further obtained by DFT. As depicted in Fig. 5h, the TTE and PF_6^- -TTE complex exhibit a lower highest occupied molecular orbital (HOMO) value compared to EMC and the PF_6^- -EMC complex, indicating that TTE possesses higher oxidative stability at the cathode surface. [14] Furthermore, the linear sweep voltammetry (LSV) curves provide solid evidence that adding TTE can mitigate the parasitic reactions between the cathode and EMC/ PF_6^- (Fig. 5i). [40].

Fig. 6 provides a comprehensive illustration of how the TTE additive enhances the electrochemical performance of graphite cathodes in DIBs.

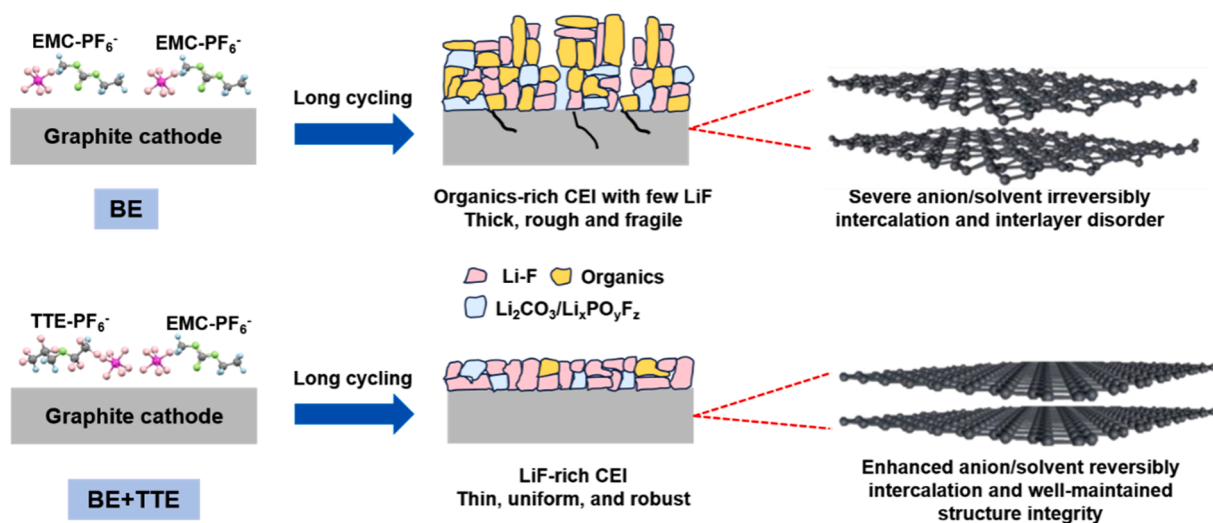


Fig. 6. Schematic illustration of the problems induced by the basic electrolyte and the stable mechanism with TTE additive.

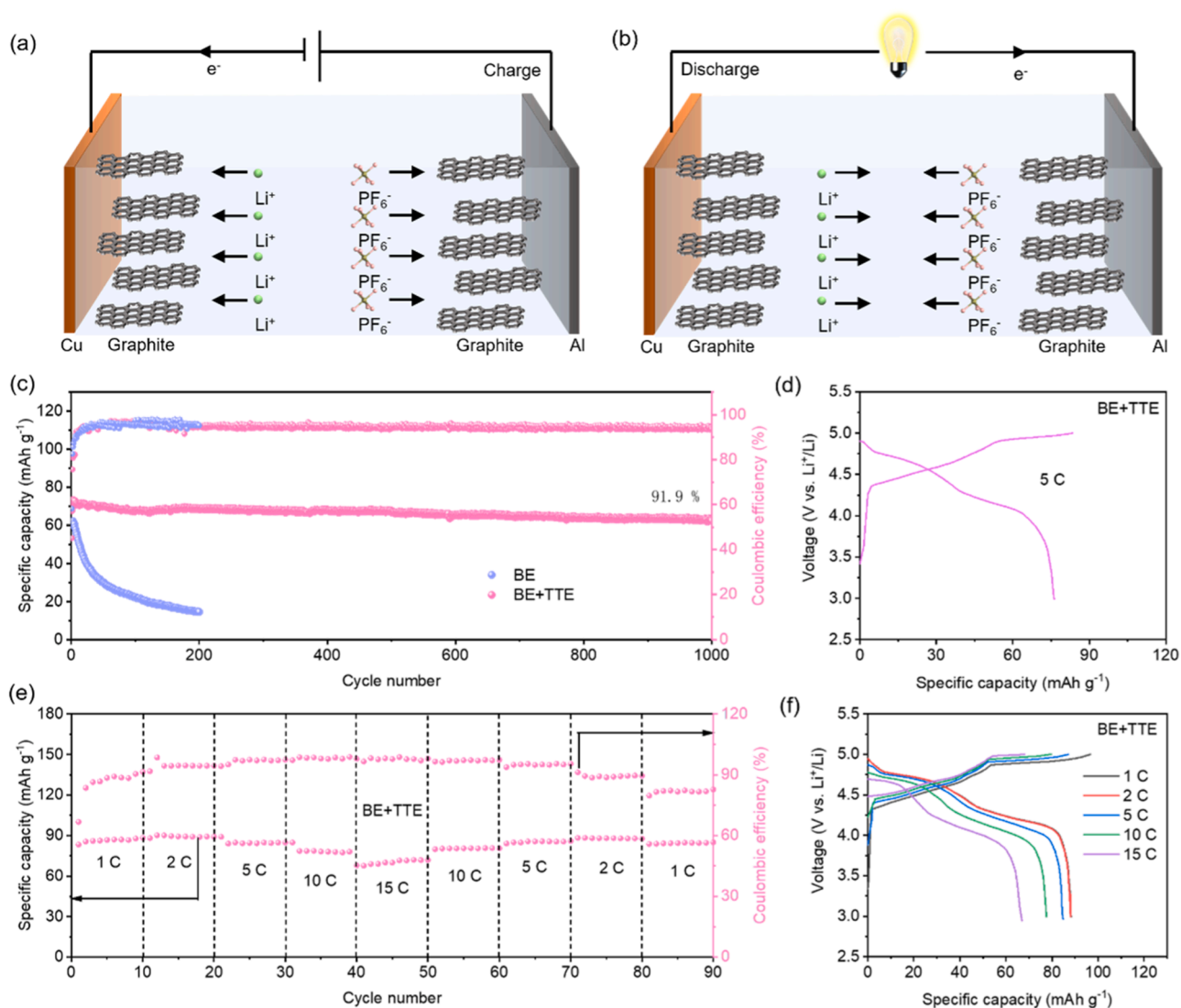


Fig. 7. (a, b) Schematic diagrams of the working mechanism of the graphite||graphite full cell. (c) Long-term cycling performance of graphite||graphite with BE and BE+TTE at 5 C with the first five cycles at 2 C. (d) Typical charge/discharge curve of graphite||graphite with BE+TTE. (e) Rate performance and (f) charge/discharge curves of graphite||graphite with BE+TTE.

In the basic electrolyte, the CEI formed by the oxidation of PF_6^- anions and solvents is thick, rough, and fragile. It mainly consists of organic components and only a few LiF. This CEI is not effective in inhibiting volume deformation of graphite during bulky anions intercalation, resulting in severe anion/solvent irreversibly intercalation and inter-layer disorder. On the other hand, TTE interacts strongly with PF_6^- anions and enters into the first shell structure of PF_6^- solvation, reducing the coordination between PF_6^- and EMC. During the charging process, the PF_6^- -TTE complex generates a thin, uniform, and robust CEI with a rich LiF component. This CEI can effectively suppress the volume change of graphite and the electrolyte oxidative decomposition, enhancing the anion (de-)intercalation reversibility and maintaining the structure integrity.

To demonstrate how TTE additives could potentially be used in DIBs, we set up graphite||graphite full cells with both BE and BE+TTE electrolytes. The working mechanisms of graphite||graphite full cells are shown in Fig. 7a and Fig. 7b. Prior to assembly, the graphite anode was pre-lithiated to form an SEI layer and reduce the initial irreversible capacity (Fig. S13). The cycling performance of the full cell was shown in Fig. 7c, while the typical charge/discharge curve with BE+TTE was presented in Fig. 7d. After 1000 cycles, the full cell with BE+TTE demonstrated a high discharge capacity of 62.5 mAh g^{-1} , 91.9 % of the first cycle. In contrast, the full cell with BE decayed rapidly within 200 cycles. Fig. 7e shows the rate performance of the full battery with BE+TTE, while Fig. 7f exhibits its charge/discharge curves at different rates. The voltage plateau is well-maintained, which confirms that DIBs have superior (de-)intercalation kinetics with BE+TTE. At 15 C, the capacity remains at 72 mAh g^{-1} , 81.5 % of the data observed at 1 C.

3. Conclusion

In summary, we have introduced TTE as a new electrolyte additive for DIBs and investigated its role in enhancing electrochemical performance. Our findings indicate that TTE preferentially enters into the first shell structure of PF_6^- solvation, improving the oxidation stability of the electrolyte and regulating the physicochemical properties of the CEI layer on the graphite cathode. This high-strength CEI layer, enriched with inorganic lithium fluoride, significantly enhances the structural stability of graphite, protects against side reactions, and improves anion transport kinetics. The Li||graphite half cell with TTE-contained electrolyte exhibits an exceptional rate capability of 95.6 % at 30 C and a long lifespan exceeding 5000 cycles at 5 C. This study sheds light on regulating anion solvation and CEI components on graphite cathodes in improving the performance of DIBs.

CRedit authorship contribution statement

Shuang Wu: Writing – original draft, Investigation, Data curation. **Xin Gu:** Writing – review & editing, Supervision, Resources, Methodology. **Yang Li:** Software. **Fengchun Li:** Formal analysis, Data curation. **Zhenjie Cheng:** Methodology. **Qian Yao:** Investigation. **Jian Yang:** Writing – review & editing. **Dandan Liu:** Methodology. **Liangjun Li:** Resources. **Pengcheng Dai:** Resources. **Mingbo Wu:** Writing – review & editing, Supervision, Resources.

Declaration of competing interest

The authors declare that they have no known competing financial interests or personal relationships that could have appeared to influence the work reported in this paper.

Data availability

Data will be made available on request.

Acknowledgements

The authors gratefully acknowledge the financial support provided by the National Natural Science Foundation of China (grant numbers 22378426 and 22138013), the Natural Science Foundation of Shandong Province (grant number ZR2022MB088), and the Taishan Scholar Project (grant number ts201712020).

Supplementary materials

Supplementary material associated with this article can be found, in the online version, at doi:10.1016/j.ensm.2024.103713.

References

- [1] H.G. Wang, Y. Wang, Q. Wu, G. Zhu, *Mater. Today* 52 (2022) 269–298.
- [2] K. Turcheniuk, D. Bondarev, G.G. Amatucci, G. Yushin, *Mater. Today* 42 (2021) 57–72.
- [3] X. Ou, D. Gong, C. Han, Z. Liu, Y. Tang, *Adv. Energy Mater.* 11 (2021) 2102498.
- [4] X. Zhou, Q. Liu, C. Jiang, B. Ji, X. Ji, Y. Tang, H.M. Cheng, *Angew. Chem. Int. Ed.* 59 (2020) 3802–3832.
- [5] Z. Sun, K. Zhu, P. Liu, H. Li, L. Jiao, *Adv. Funct. Mater.* 31 (2021) 2107830.
- [6] T. Placke, A. Heckmann, R. Schmich, P. Meister, K. Beltróp, M. Winter, *Joule* 2 (2018) 2528–2550.
- [7] J. Hao, X. Li, X. Song, Z. Guo, *EnergyChem* 1 (2019) 100004.
- [8] X. Han, G. Xu, Z. Zhang, X. Du, P. Han, X. Zhou, G. Cui, L. Chen, *Adv. Energy Mater.* 9 (2019) 1804022.
- [9] Y. Sui, C. Liu, R.C. Masse, Z.G. Neale, M. Atif, M. AlSalhi, G. Cao, *Energy Storage Mater.* 25 (2020) 1–32.
- [10] W.H. Li, Q.L. Ning, X.T. Xi, B.H. Hou, J.Z. Guo, Y. Yang, B. Chen, X.L. Wu, *Adv. Mater.* 31 (2019) 1804766.
- [11] X. Fan, C. Wang, *Chem. Soc. Rev.* 50 (2021) 10486–10566.
- [12] L. Zhang, H. Wang, X. Zhang, Y. Tang, *Adv. Funct. Mater.* 31 (2021) 2010958.
- [13] K.V. Kravchik, P. Bhauriyal, L. Piveteau, C.P. Guntlin, B. Pathak, M.V. Kovalenko, *Nat. Commun.* 9 (2018) 4469.
- [14] S. Tao, B. Demir, A. Baktash, Y. Zhu, Q. Xia, Y. Jiao, Y. Zhao, T. Lin, M. Li, M. Lyu, *Angew. Chem. Int. Ed.* 62 (2023) e202307208.
- [15] F. Li, X. Gu, A. Cui, Y. Li, S. Dong, S. Wu, Z. Cheng, Q. Yao, J. Yang, M. Wu, *Adv. Funct. Mater.* 34 (2024) 2313146.
- [16] L. Xiang, X. Ou, X. Wang, Z. Zhou, X. Li, Y. Tang, *Angew. Chem. Int. Ed.* 59 (2020) 17924–17930.
- [17] X. Tong, X. Ou, N. Wu, H. Wang, J. Li, Y. Tang, *Adv. Energy Mater.* 11 (2021) 2100151.
- [18] N. Sun, R. Li, Y. Zhao, H. Zhang, J. Chen, J. Xu, Z. Li, X. Fan, X. Yao, Z. Peng, *Adv. Energy Mater.* 12 (2022) 2200621.
- [19] D. Yu, Q. Zhu, L. Cheng, S. Dong, X. Zhang, H. Wang, N. Yang, *ACS Energy Lett* 6 (2021) 949–958.
- [20] Y. Wang, Y. Zhang, S. Wang, S. Dong, C. Dang, W. Hu, D.Y. Yu, *Adv. Funct. Mater.* 31 (2021) 2102360.
- [21] Z. Cheng, L. Guo, Q. Dong, C. Wang, Q. Yao, X. Gu, J. Yang, Y. Qian, *Adv. Energy Mater.* 12 (2022) 2202253.
- [22] C. Chen, C.-S. Lee, Y. Tang, *Nano-Micro Lett* 15 (2023) 121.
- [23] D.M. Driscoll, S.N. Lavan, M. Zorko, P.C. Redfern, S. Ilic, G. Agarwal, T.T. Fister, R. S. Assary, L. Cheng, D. Strmcnik, *Chem* 9 (2023) 1955–1971.
- [24] X. Ren, S. Chen, H. Lee, D. Mei, M.H. Engelhard, S.D. Burton, W. Zhao, J. Zheng, Q. Li, M.S. Ding, *Chem* 4 (2018) 1877–1892.
- [25] Q. Liu, Y.H. Feng, X. Zhu, M. Liu, L. Yu, G.X. Wei, X.Y. Fan, X. Ji, P.F. Wang, H. Xin, *Nano Energy* 123 (2024) 109389.
- [26] W.H. Li, Y.M. Li, X.F. Liu, Z.Y. Gu, H.J. Liang, X.X. Zhao, J.Z. Guo, X.L. Wu, *Adv. Funct. Mater.* 32 (2022) 2201038.
- [27] D. Guan, W. Wang, B. Chen, J. Wu, G. Hu, Z. Peng, Y. Cao, L. Wen, K. Du, *Adv. Funct. Mater.* 33 (2023) 2215113.
- [28] H. Tan, D. Zhai, F. Kang, B. Zhang, *Carbon* 178 (2021) 363–370.
- [29] B. Ji, F. Zhang, X. Song, Y. Tang, *Adv. Mater.* 29 (2017) 1700519.
- [30] I.A. Rodríguez-Pérez, Z. Jian, P.K. Waldenmaier, J.W. Palmisano, R. S. Chandrabose, X. Wang, M.M. Lerner, R.G. Carter, X. Ji, *ACS Energy Lett* 1 (2016) 719–723.
- [31] L. Fan, Q. Liu, Z. Xu, B. Lu, *ACS Energy Lett* 2 (2017) 1614–1620.
- [32] L.N. Wu, J. Peng, Y.K. Sun, F.M. Han, Y.F. Wen, C.G. Shi, J.J. Fan, L. Huang, J.T. Li, S.G. Sun, *ACS Appl. Mater. Interfaces* 11 (2019) 18504–18510.
- [33] H. Jiang, X. Han, X. Du, Z. Chen, C. Lu, X. Li, H. Zhang, J. Zhao, P. Han, G. Cui, *Adv. Mater.* 34 (2022) 2108665.
- [34] J. Hu, W. Huang, L. Yang, F. Pan, *Nanoscale* 12 (2020) 15036–15044.
- [35] M.Á. Muñoz-Márquez, D. Saurel, J.L. Gómez-Cámer, M. Casas-Cabanas, E. Castillo-Martínez, T. Rojo, *Adv. Energy Mater.* 7 (2017) 1700463.
- [36] G. Wang, M. Yu, X. Feng, *Chem. Soc. Rev.* 50 (2021) 2388–2443.
- [37] R. Kempaiah, G. Vasudevamurthy, A. Subramanian, *Nano Energy* 65 (2019) 103925.
- [38] Y. Qin, K. Xu, Q. Wang, M. Ge, T. Cheng, M. Liu, H. Cheng, Y. Hu, C. Shen, D. Wang, *Nano Energy* 96 (2022) 107082.
- [39] H.J. Guo, H.X. Wang, Y.J. Guo, G.X. Liu, J. Wan, Y.X. Song, X.A. Yang, F.F. Jia, F. Y. Wang, Y.G. Guo, *JACS* 142 (2020) 20752–20762.

- [40] Y. Wang, Y. Zhang, S. Dong, W. Zhou, P.K. Lee, Z. Peng, C. Dang, P.H.L. Sit, J. Guo, D.Y. Yu, *Adv. Energy Mater.* 12 (2022) 2103360.
- [41] Y. Zhao, K. Xue, D.Y. Yu, *Adv. Funct. Mater.* 33 (2023) 2300305.
- [42] K. Kim, H. Ma, S. Park, N.-S. Choi, *ACS Energy Lett* 5 (2020) 1537–1553.
- [43] Z. Zhang, X. Wang, Y. Bai, C. Wu, *Green Energy Environ* 7 (2022) 606–635.
- [44] C. Yang, X. Liao, X. Zhou, C. Sun, R. Qu, J. Han, Y. Zhao, L. Wang, Y. You, J. Lu, *Adv. Mater.* 35 (2023) 2210966.
- [45] P. Bai, X. Ji, J. Zhang, W. Zhang, S. Hou, H. Su, M. Li, T. Deng, L. Cao, S. Liu, *Angew. Chem. Int. Ed.* 61 (2022) e202202731.
- [46] L. Suo, O. Borodin, T. Gao, M. Olguin, J. Ho, X. Fan, C. Luo, C. Wang, K. Xu, *Science* 350 (2015) 938–943.
- [47] Y. Wu, A. Wang, Q. Hu, H. Liang, H. Xu, L. Wang, X. He, *ACS Central Sci* 8 (2022) 1290–1298.
- [48] Z. Cheng, Q. Dong, G. Pu, J. Song, W. Zhong, J. Wang, *Small* (2024) 2400389.
- [49] L. Chen, H. Zhang, R. Li, S. Zhang, T. Zhou, B. Ma, C. Zhu, X. Xiao, T. Deng, L. Chen, *Chem* 10 (2024) 1196–1212.
- [50] D. Wu, C. Zhu, H. Wang, J. Huang, G. Jiang, Y. Yang, G. Yang, D. Tang, J. Ma, *Angew. Chem. Int. Ed.* 63 (2024) e202315608.